Local probe of irradiation-induced structural changes and orbital magnetism in Fe$_{60}$Al$_{40}$ thin films via an order-disorder phase transition

Enrico La Torre,[1,*] Alevtina Smekhova,[2,†] Carolin Schmitz-Antoniak,[2] Katharina Ollefs,[1] Benedikt Eggert,[1] Birte Cöster,[1]
Dirk Walecki,[1] Fabrice Wilhelm,[3] Andrei Rogalev,[3] Jürgen Lindner,[4] Rantej Bali,[4] Rudra Banerjee,[5]
Biplab Sanyal,[5] and Heiko Wende[1]

[1]*Fakultät für Physik, Universität Duisburg-Essen und CENIDE, D-47057 Duisburg, Germany*
[2]*Peter Grünberg Institut (PGI-6), Forschungszentrum Jülich, D-52425 Jülich, Germany*
[3]*European Synchrotron Radiation Facility (ESRF), BP 220, 38043 Grenoble Cedex 9, France*
[4]*Institut für Ionenstrahlphysik und Materialforschung, Helmholtz-Zentrum Dresden-Rossendorf, D-01328 Dresden, Germany*
[5]*Department of Physics and Astronomy, Uppsala University, SE-75120 Uppsala, Sweden*

Hard x-ray absorption and magnetic circular dichroism spectroscopy have been applied to study the consequential changes of the local environment around Fe atoms and their orbital polarizations in 40 nm thick Fe$_{60}$Al$_{40}$ thin films along the order-disorder ($B2 \rightarrow A2$) phase transition initiated by 20-keV Ne$^+$ ion irradiation with fluences of $(0.75–6) \times 10^{14}$ ions cm^{-2}. The analysis of the extended x-ray absorption fine structure spectra measured at the Fe K edge at room temperature revealed an increased number of Fe-Fe nearest neighbors from 3.47(7) to 5.0(1) and $\sim1\%$ of volume expansion through the transition. The visualization of the Fe and Al nearest-neighbor rearrangement in the first coordination shell of Fe absorbers via the transition was carried out by wavelet transformations. The obtained changes in Fe coordination are evidently reflected in the x-ray magnetic circular dichroism spectra which show an increased orbital magnetic moment of Fe atoms and a pronounced magnetic multielectronic excitations peak at ~60 eV above the edge. The amplitudes of both peaks demonstrated similar dependencies on the irradiation fluence. The results of self-consistent density functional calculations on relaxed Fe$_{60}$Al$_{40}$ model structures for the ordered ($B2$) and the disordered ($A2$) phases are consistent with the experimental findings and point to the formation of Fe-rich regions in the films studied.

I. INTRODUCTION

An intention of having complex structures with different configurations of lateral magnetic properties for use in ultra-high-density magnetic recording applications and spintronic devices has stimulated the search for techniques and materials that could fulfill the necessary requirements. Long ago, ion irradiation in combination with lithographic techniques was established to be a powerful tool from this perspective [1]. Tailoring the magnetic properties of thin films can be achieved via launching structural phase transition by irradiation, leading to the final ordered or disordered states, which reveal either increased or decreased magnetization depending on the material used [2,3].

Among a broad range of alloys that exhibit a ferromagnetic long-range ordering in the final disordered phase, transition-metal aluminides Fe-Al have attracted a lot of attention in past decades due to their unique magnetic behavior that could be rather easily tuned. It has been demonstrated that specific features of a well-pronounced ferromagnetic order are strongly dependent on a particular stoichiometry, the degree of the chemical disorder, the lattice parameter, and the presence of defects in the crystal structure [2,4–8]. The particular

Fe-rich alloy of Fe$_{60}$Al$_{40}$ (at.%) composition exhibits the most stable chemically ordered $B2$ phase (CsCl crystal structure) that is paramagnetic at room temperature (RT) and can be transformed into the ferromagnetic chemically disordered $A2$ phase (body centered cubic [bcc] crystal structure) by various methods like ball milling [6], cold working [9], high-pressure compression [10], and ion irradiation [8,11,12]. Nowadays, by exploiting this phase transition it is possible to create different magnetic structures with locally adjusted magnetic properties on the base of Fe$_{60}$Al$_{40}$ thin films that may be used in spin transport and memory devices [11,12], which can even have a laser-assisted on-off switching of magnetization [13]. Patterning by ion irradiation with a low fluence through a lithographic mask can achieve sub-50-nm resolution [8], while by means of He/Ne ion microscope even better lateral resolution is expected. In addition to a great interest in Fe$_{60}$Al$_{40}$ thin films from a practical point of view, there are also a number of fundamental questions related to peculiarities of the local environment, lattice distortions, charge transfer, and magnetic polarizations as well as their specific changes under the ion irradiation within this new type of objects.

Ion beam irradiation with low fluences (up to 10×10^{15} ions cm^{-2}) can be effectively used for creation of the chemical disorder in films of different thicknesses. Depending on their kinetic energy, ions can penetrate the entire volume of the film and the density of induced defects can be changed by increasing the irradiation fluence [8,14]. The amount of

---

*enrico.la-torre@stud.uni-due.de
†a.smekhova@fz-juelich.de

024101-1

induced defects is proportional to the degree of the chemical disorder, which is represented by vacancies created by Fe and Al atoms knocked from their initial positions in the ordered $B2$ phase. Due to thermal diffusion, these vacancies are filled back, resulting in the formation of the disordered $A2$ phase. The profile of the created vacancies and the related chemical disorder follows a Gaussian distribution with a maximum at a certain depth; nevertheless, depending on the irradiation energy, a much more homogeneous profile of the magnetization could be reached as, for instance, in $Fe_{60}Al_{40}$ thin films of 40 nm thickness irradiated by 15–30 keV Ne^+ ions [8,14]. According to Tahir *et al.* [15], films prepared in such a way exhibit a simultaneous magnetization reversal over the whole film thickness under an applied magnetic field. However, the details of the formation mechanism of a disorder-induced ferromagnetism in $Fe_{60}Al_{40}$ thin films are still unclear.

A description of magnetization variations in FeAl alloys induced by chemical disorder is usually based on the local environment model [16,17]. In this model, the value of Fe magnetic moment depends on the number of Fe-Fe nearest-neighbor atoms and has a tendency of the Fe moment increasing for larger numbers of the nearest Fe neighbors: The largest magnetic moment is expected for a number of Fe-Fe nearest neighbors of more than five and for less nearest-neighboring Fe-Fe atoms the magnetic moment drastically decreases [18]. Moreover, changes of the lattice parameter can contribute significantly: As demonstrated by Nogués *et al.* [2], up to 40% of Fe magnetic moment can be attributed to lattice expansion effects during the disordering process. Band structure calculations have revealed a strong influence of structural defects and lattice distortions on the ferromagnetic coupling within the disordered $A2$ phase [19,20]. It is evident from above that the peculiarities in the local coordination of FeAl alloys play an important role in the formation of its ferromagnetic order. Therefore, the detailed studies of the local coordination of Fe atoms in $Fe_{60}Al_{40}$ thin films via $B2 \rightarrow A2$ phase transition can be considered as the first necessary step in understanding their magnetic properties.

X-ray absorption spectroscopy (XAS) with polarized x rays from a synchrotron radiation source is an effective tool to probe the local environment, electronic structure, and magnetic properties of an absorbing atom in an element-specific way. Detailed studies performed on a local scale can clarify hidden mechanisms of disorder-induced ferromagnetism phenomena in $Fe_{60}Al_{40}$ via understanding the influence of the local surrounding and features of Fe-Al hybridization on the magnetic properties. Extended x-ray absorption fine structure (EXAFS) is a unique signature of the absorber embedded in a particular surrounding. EXAFS at K absorption edges can probe the characteristic features of atom coordination and is effectively exploited for studies of slight changes in the local surrounding and their peculiarities due to transitions from spherically symmetric s states ($1s \rightarrow np$). A common EXAFS analysis provides information about the number of inequivalent neighbors in the several first coordination shells of the absorbing atom and their effective interatomic distances (R). There are only a few reports in literature dedicated to detailed EXAFS analysis applied to FeAl alloys of different stoichiometry [21,22] and to FeAl multilayers mixed by ion irradiation [23]. An additional analysis, so-called wavelet transforms (WT) analysis [24], can

be applied for distinguishing the contributions from different backscatters of the complex compound in the first coordination shell of a particular absorber. As a result, three-dimensional (3D) WT (R, k) plots visualize distinct distributions of effective radial distances associated with a particular wave number k and, hence, with a particular element that acts as a backscatter.

X-ray magnetic circular dichroism (XMCD) technique applied for K edges provides a very sensitive tool for *magnetic* probe of slight local variations. In spite of an *a priori* tiny signal, this technique has been widely used for magnetic studies of bulk-like properties in recent decades [25]. In the case of $Fe_{60}Al_{40}$ thin films, a noticeable growth of the XMCD amplitude associated with Fe $4p$ states orbital polarization is expected to be found through the phase transition. According to numerous prior Mössbauer spectroscopy (MS) studies of ball-milled FeAl alloys, only a slightly varied number of Fe and Al atoms around ^{57}Fe absorber provides significant changes in the magnetic hyperfine fields of iron nucleus that reflect the strong changes in spin polarizations of core s and p electrons. As a consequence, any rearrangements in the first coordination shell of Fe atoms should be reflected in Fe orbital magnetic polarizations due to spin-orbit coupling and thus could be probed by XMCD technique at the Fe K edge.

An additional advantage of XMCD technique exploited at K edges is a possibility to detect a dichroic signal that relates to magnetic multielectronic excitations (MEE, secondary processes), and in such a way to probe the magnetism of unoccupied $3d$ states with hard x rays. The energy position of Fe MEE peak is around $\sim$60 eV above the absorption edge and can be described by super-Coster-Kronig $3p \rightarrow 3d$ transitions going simultaneously with $\epsilon p \rightarrow 3d$ de-excitation, resulting in $(1s)^1(3p)^5(3d)^{n+2}$ final state [26,27]. In the case of pure iron, the amplitude of the MEE dichroic signal is comparable with the XMCD signal at the K edge, has an opposite sign, and is about $\sim$10^{-3} of the photoabsorption intensity. Qualitatively, the intensity of this dichroic signal was found to be proportional to Fe magnetic moment in a series of different compounds [26].

Preceding first-principles calculations, applied for transition-metal aluminides of different stoichiometry [7,19,28–31], allow one to draw a number of conclusions about variations of the lattice parameter, the electronic structure, local magnetic moments, and a charge transfer from Al to the transition metal (TM) d shell considering different local environments in the ordered $B2$ phase. The most efforts have been spent on configurations when a TM atom was placed on the Al site position (so-called "antisite defect" which is typical for Fe-rich systems at RT) or when a vacancy was considered on an initially transition-metal site (the case of Al-rich systems or Fe-rich alloys at low temperatures). According to the literature, good agreement with experimental data has been found in most of the models. Nevertheless, not all of these studies have been performed by self-consistent calculations, which take the relaxation processes due to variations in local configurations into account.

In our paper, we focus on consequential structural changes and related variations of Fe orbital polarizations in 40 nm thick $Fe_{60}Al_{40}$ thin films irradiated by 20 keV Ne^+ ions with different fluences that initiate the order-disorder phase transition. The degree of chemical disorder induced by ion irradiation via smooth variation of Fe-Fe nearest neighbors, changes of

interatomic distances, and orbital atomic polarizations have been probed locally by XAS and XMCD at the Fe K edge at RT. An analysis of EXAFS oscillations reveals the clear rearrangement of a particular number of Fe and Al nearest neighbors in the first and second coordination shells around the absorbing Fe atom together with an expansion of the unit cell through the full order-disorder ($B2 \rightarrow A2$) phase transition. Wavelet transforms were used to additionally visualize the rearrangement of Fe-Fe and Fe-Al nearest neighbors via the transition. XMCD spectra show a clear rise of orbital magnetic moment of Fe atoms with increase of the chemical disorder and the appearance of a pronounced magnetic MEE peak. Theoretical support has been provided by *ab initio* self-consistent density functional (DFT) calculations on relaxed $Fe_{60}Al_{40}$ structures in the ordered $B2$ and the disordered $A2$ states. The results of these studies could be expanded on understanding the disorder-induced ferromagnetism phenomenon in other TM alloys as well.

A. Extended x-ray absorption fine structure

A short introduction to the EXAFS technique and its analysis by conventional Fourier and novel wavelet transformation is given in this subsection to underpin the experimental studies of Fe local environment that play a crucial part within this work.

EXAFS refers to the oscillatory behavior of the x-ray absorption coefficient in the energy range of about 100–1000 eV above the absorption edge. In a simplistic picture, these oscillations occur due to interference effects between forward-propagating waves created by an ejected photoelectron (emerged due to an absorption of the x-ray photon) and waves scattered back from the neighboring atoms at the site of the absorbing atom. For a particular energy of the created photoelectron, the amplitude of these interference oscillations depends on the number and type of neighboring atoms, their distances from the central absorbing atom, and structural (static and dynamic) disorders. This makes it possible to determine the chemical local environment of the absorbing atom by analysis of the EXAFS oscillations $\chi(k)$.

The resulting $\chi(k)$ is a sum of all backscattering contributions, whose envelope function depends on the scattering path of the photoelectron (including single- and multiple-scattering effects) and the backscattering atoms. The mathematical expression of all contributions could be found in the Supplemental Material [32]. The wave number k of the photoelectron is related to its energy E as $k = \sqrt{2m(E - E_0)/\hbar^2}$, where E_0 and m is the binding energy and the mass of the photoelectron, respectively. In most cases the analysis of $\chi(k)$ frequencies allows one to establish particular details of the local environment around the absorbing atom with high precision.

1. Fourier transform

The most common technique for EXAFS analysis exploits the Fourier transform (FT), as it was first described by Sayers *et al.* [33] in 1971. The FT of $\chi(k)$ oscillations retrieves a pseudoradial distribution function with peaks in R space, which are in the first approximation related to the distances between backscattering atoms and the central absorbing atom.

Since the photoelectron accumulates a phase shift during each scattering event, the positions of FT peaks are shifted with respect of the real interatomic distances of backscattering atoms. Thus, a correct interpretation of the FT results is not trivial and needs the use of theoretical standards. This could be achieved by a comparison of the experimental $k\chi(k)$ and $|FT(k\chi(k))(R)|$ data with the simulated one using FEFF9 considering a model structure. For further reading, a review can be found, e.g., in Ref. [34].

2. Wavelet transform

An alternative to the Fourier transform, which may overcome some of the FT shortcomings, is the so-called wavelet transformation (WT). For the WT, the infinitely extended periodic oscillations in the FT are replaced by a scalable and translatable located Gaussian wave packet, which then acts as an integral transformation kernel. As a result, the WT provides information about individual wave numbers k related to a particular maxima in R space together with their contributions to the magnitude of the total FT ($|FT(k\chi(k))(R)|$). In this way, contributions from different k values but with the same oscillation frequencies, which is the case for altered backscatters, could be separated and presented as shown in the 3D $WT(R,k)$ plots.

In this respect, the key parameter for the utility of the WT procedure is the backscattering amplitude $F(k)$ of neighboring atoms. Since $F(k)$ enters the EXAFS oscillations as a factor, it is directly imprinted on the $\chi(k)$ envelope function with a maximum around the k value related to a maximum of the backscattering amplitude $F(k)$. In the case of Fe and Al, the positions of $F(k)$ maxima are well separated [see Fig. 1(a)] and are clearly resolved in the WT plots, as it will be shown below. Thus, it is possible to distinguish between contributions from these two elements. Another important parameter of the backscatters is the EXAFS phase $\Phi(k)$, which in the case of Fe and Al elements has a nonlinear k dependence, as shown in Fig. 1(b). The phase factor of each element gives an input into the total phase shift of the photoelectron scattering event resulting in a shift of maxima in both FT and WT as a function of R. However, in the case of the WT, the k dependence of this shift is resolved, leading to an inclined WT magnitude [35]. A review on this topic can be found, e.g., in Refs. [24,35].

II. EXPERIMENTAL AND COMPUTATIONAL DETAILS

A. Samples

$Fe_{60}Al_{40}$ thin films of 40 nm thickness were prepared on SiO_2/Si(001) substrates by magnetron sputtering at RT with further annealing and ion irradiation as described by Bali *et al.* [8]. The deposition was performed using a target of the same Fe-rich composition. Annealing in vacuum at 773K for 1 h leads to the formation of the chemically ordered $B2$ phase that was confirmed by the observed superlattice (100) XRD peak [8,36]. The native oxide SiO_2 buffer layer was used to prevent an unfavorable silicide formation at the $Fe_{60}Al_{40}$/Si interface during the annealing process. The irradiation by 20-keV Ne^+ ions with fluences up to 6×10^{14} ions cm^{-2} destroys the chemical ordering while preserving a structural integrity of the films and, thus, allows one to create a number of $A2$ phases with different degrees of chemical disorder.
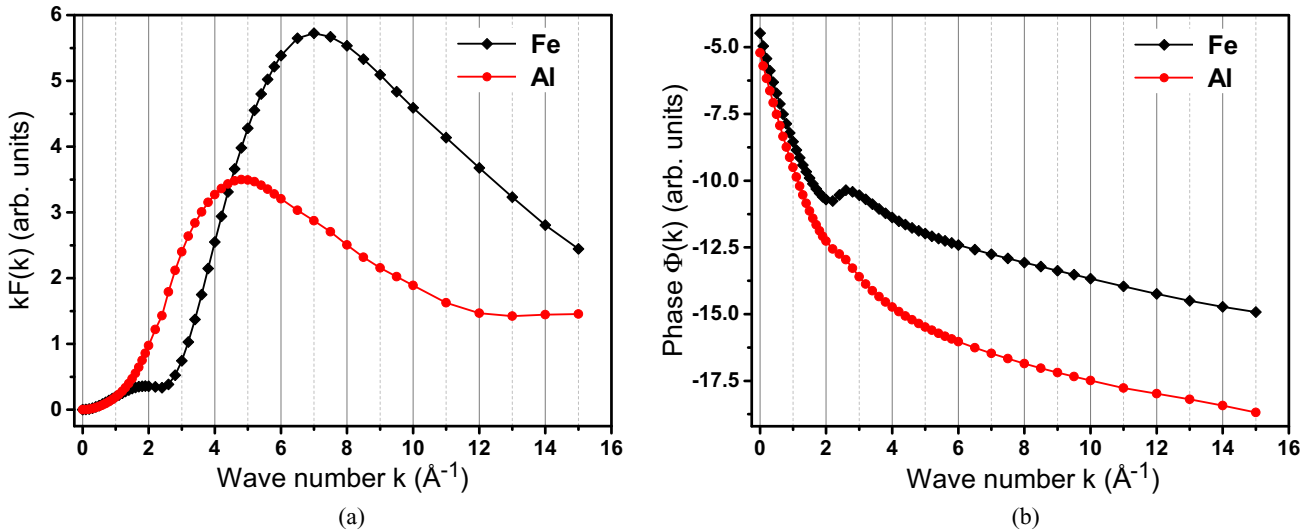
FIG. 1. (a) Calculated backscattering amplitudes F(k) weighted with k for Fe and Al atoms in $Fe_{60}Al_{40}$ model structure using FEFF9. The peak positions are important for the interpretation of the further wavelet transforms WT(R,k). (b) The calculated phase factors $\Phi(k)$ of the backscattering Fe and Al atoms in the same model structure. The nonlinearity of $\Phi(k)$ leads to the rotated maxima in the WT(R,k) plots.

In our work, three different types of samples have been studied. The annealed one that has not been irradiated was used as a reference for the chemically ordered $B2$ phase. The "disorder-gradient" sample, prepared by a continuous increase of Ne^+ irradiation fluence of $0–3 \times 10^{14}$ ions cm^{-2} along the film surface with the help of an *in situ* shutter moved in steps of ~100 μm, represents the intermediate $A2$ states via the order-disorder transition and offers possible insights into the particular changes in the local structure through the transition: Increase of the irradiation fluence provides a smooth rise of chemical disorder that should be followed by variations in Fe-Fe nearest neighbors, interatomic distances, and magnetic moments. The sample uniformly irradiated with the highest fluence of 6×10^{14} ions cm^{-2} was used as a representative of the fully disordered $A2$ state.

B. X-ray absorption measurements

Element-specific EXAFS measurements have been performed at the polarization-dependent absorption beamline ID12 at the ESRF (Grenoble, France) [37]. EXAFS spectra were recorded at the Fe K absorption edge with linearly polarized x rays at room temperature in the total fluorescence yield (TFY) detection mode and 45 deg incidence geometry. The chosen detection mode allows one to study thin films on substrates nondestructively and without any additional preparation steps before the measurements. The resulting spectra were taken in the range of more than 800 eV above the absorption edge with energy steps ~0.5 eV. XMCD spectra were taken for two opposite circular polarizations of incoming x rays as a direct difference of absorption spectra by flipping an external magnetic field of ±0.9 T along the beam direction. The degree of the circular polarization of photons was around 98%. The value of applied magnetic field was high enough to fully saturate the films in the chosen experimental geometry. During the spectra acquisition, the undulator parameters were smoothly adjusted to get the same level of signal-to-noise ratio before and well above the absorption edge. Element-specific

magnetization loops have been measured as field dependence of the XMCD maximum. The fluorescence signal from 4-μm Ti foil was used to monitor the intensity of incoming x-ray beam and was necessary for the proper data analysis. Due to a high penetration depth of incoming x-ray photons and a large probing depth of the fluorescence yield, the observed magnetic signal represents an averaged magnetic moment of Fe atoms over the whole film thickness.

C. DFT calculations

To study the effects of chemical disorder on structural, electronic, and magnetic properties in $Fe_{60}Al_{40}$ model crystals from a theoretical point of view, first-principles density functional calculations have been performed employing the VASP [38–41] code based on the plane-wave basis and the projector augmented wave method to describe electron-ion interactions. The method has been applied for an $Fe_{60}Al_{40}$ alloy in the chemically ordered and fully disordered phases. The lattice parameter and the space group for the model crystal were set to 2.858 Å and 221 (bcc), respectively. The cut-off energy for the plane waves was set to 400 eV, the forces were converged to 0.01 eV/Å, and a $3 \times 3 \times 3$ k-point mesh was used for the integration over the Brillouin zone. In addition, the SPR-KKR code based on Korringa-Kohn-Rostoker method coupled with coherent potential approximation (KKR-CPA) [42,43] has been used to have a comparison with the results obtained from VASP calculations that took into account a relaxation of atomic positions, which is extremely difficult to perform with KKR method. For both calculations, the Perdew-Burke-Ernzerhof exchange-correlation potential was employed; however, VASP calculations were performed with a scalar relativistic Hamiltonian whereas a fully relativistic Dirac Hamiltonian has been considered for SPR-KKR calculations.

It is important to note that due to Fe-rich stoichiometry, the chemically ordered $B2$ phase of $Fe_{60}Al_{40}$ has a fraction of Fe atoms in the initially pure Al lattice planes assumed for $Fe_{50}Al_{50}$. These excess Fe atoms have a chemically ordered

environment within the neighboring initially pure Fe planes, and vice versa. Multiple configurations with different total energies for this ordered $B2$ phase are possible. Among considered 10 configurations, the configuration with minimum ground-state energy (E_g) was chosen for the further studies of electronic density of states (DOS) and magnetic properties presented later in this paper. For all these calculations, the internal coordinates have been relaxed, keeping the lattice parameter fixed; a $5 \times 5 \times 5$ supercell was used. The model crystal for the fully disordered $A2$ phase was generated with a special quasirandom structure (SQS) [44] method; thus, in this case it is enough to consider only one configuration in VASP calculations that represents a homogeneous disorder. SPR-KKR calculations have been done within CPA for configuration averaging.

III. RESULTS AND DISCUSSION

The experimental EXAFS spectra and extracted $k\chi(k)$ dependence for all samples are shown in Figs. 2(a) and 2(b). Clear changes in the amplitude and the shape of EXAFS oscillations are visible for samples in $B2$ and different $A2$ states. For all spectra, the difference between the absorption signal and the background function becomes very small for wave numbers $k > 10$ Å^{-1}, so the noise in the signal and artifacts from removing Bragg reflection peaks become visible. To obtain a radial distance from the Fe absorbing atom to absorbers in the first coordination shell, the Fourier transform has been done within the Hanning window function starting at $k_{\min} = 3.3$ Å^{-1} and ending at $k_{\max} = 12.3$ Å^{-1} ($\Delta k = 9$ Å^{-1}, $dk = 0.1$ Å^{-1}).

The results of such a Fourier transformation of EXAFS data are shown in Fig. 2(c). Since the Fourier transform is not phase corrected, only the effective radial distances (R) to the absorbing Fe atom are shown. Therefore, the positions of the maxima between $R = 1.5$ Å and $R = 6$ Å refer only to effective distances of backscattering atoms in the first two coordination shells. Note that for the chemically ordered sample, a pronounced minimum at $R = 2$ Å is presented which vanishes completely for samples with disorder. The most pronounced peak around $R = 2.45$ Å exhibits a small shift in its position depending on the degree of the chemical disorder while for distances $R > 3$ Å only changes in the magnitude of the Fourier transform have been found.

A. Local coordinations

1. Results of wavelet transforms

The WT reveals at which wave number in the EXAFS oscillations the maxima of the Fourier transform are being generated. In order to construct a proper model system, information about the local surrounding of the absorbing Fe atom is necessary. Knowledge of the energy dependence of the backscattering amplitude, which was presented in Fig. 1(a), makes the interpretation of the WT possible.

In Fig. 3, the WTs of the EXAFS spectra from the annealed, "disorder-gradient," and homogeneously irradiated samples are shown. The WTs have been performed for $k\chi(k)$
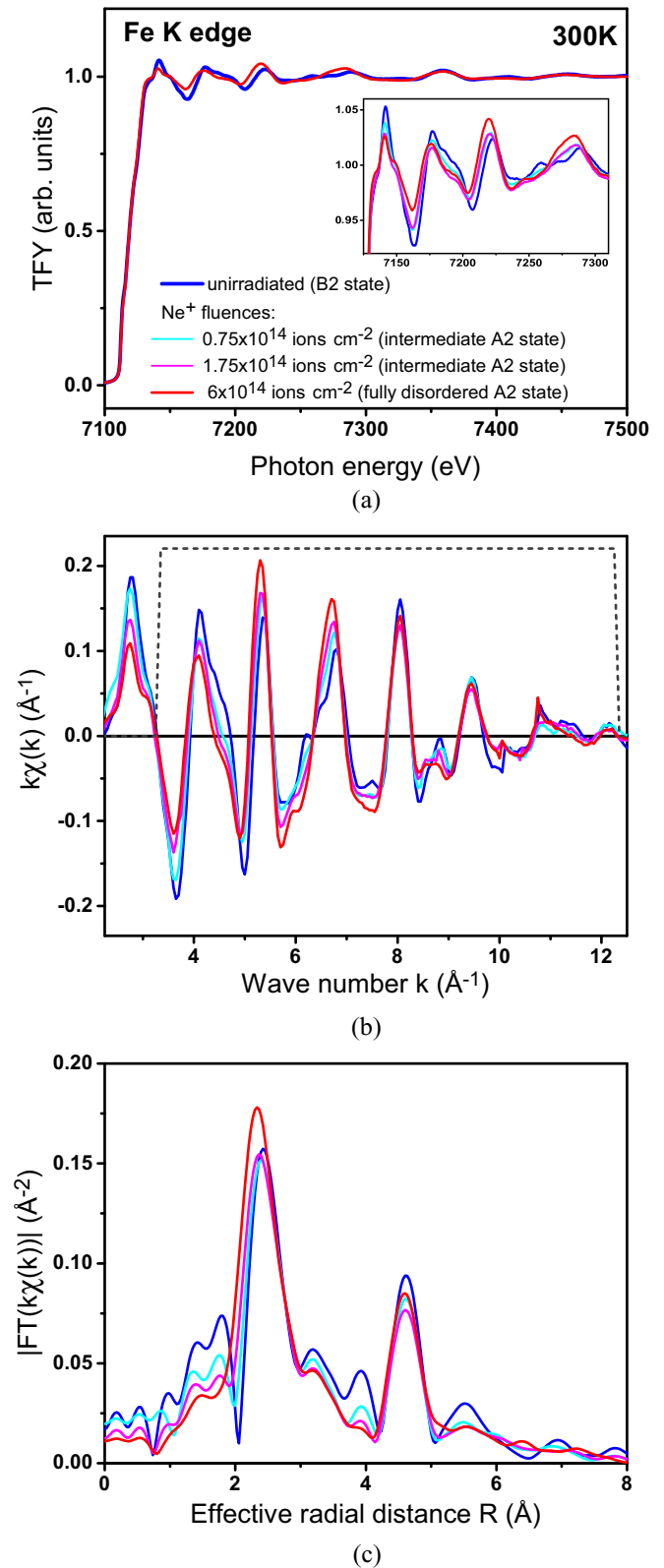

FIG. 2. (a) Experimental EXAFS spectra of the studied samples recorded at the Fe K edge and room temperature, (b) extracted EXAFS oscillations $\chi(k)$ weighted with k, and (c) their Fourier transforms $|FT(k\chi(k))(R)|$. The degree of the chemical disorder increases from blue to red; with an increasing of the chemical disorder the minimum of $|FT(k\chi(k))(R)|$ at $R = 2$ Å vanishes.
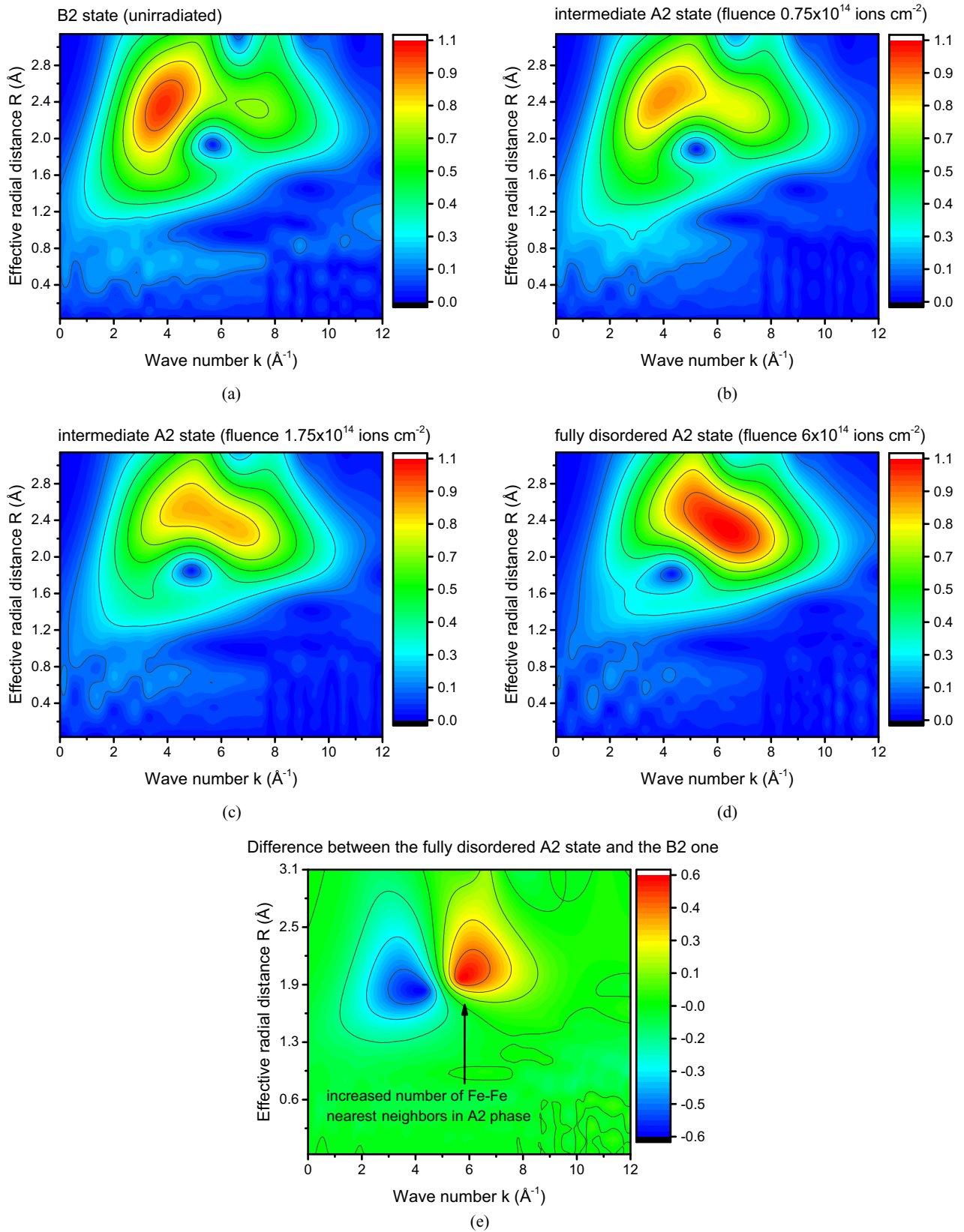
FIG. 3. Normalized wavelet transforms WT(R,k) of $k\chi(k)$ of the annealed (unirradiated) sample (a), the "disorder-gradient" sample irradiated with fluences of 0.75×10^{14} ions cm^{-2} (b) and 1.75×10^{14} ions cm^{-2} (c), and the sample uniformly irradiated with the highest fluence of 6×10^{14} ions cm^{-2} (d). The radial distance axis (R) represents only an effective distance since the wavelet transform function WT(R,k) is not phase corrected; a relocation of WT(R,k) maxima along the $B2 \rightarrow A2$ transition is clearly visible. The difference of the WT presented in panels (d) and (a) is shown in panel (e).

dependence with $k \geqslant 2.5$ Å^{-1}. This range of k values ensures that only the main peak of the backscattering amplitude of Fe at $k = 7$ Å^{-1} contributes in the WT without any interference with a minor prepeak at $k = 1.9$ Å^{-1} [see Fig. 1(a)]. Even more important, in this case the influence of the x-ray absorption near-edge structure is significantly reduced (in analogy to the choice of the window function for the FT). The amplitudes of each WT plot have been normalized to the maximum value of WT for the ordered $B2$ state.

The evolution of the WT shapes and amplitudes with increasing of chemical disorder is clearly visible. In the chemically ordered $B2$ state [Fig. 3(a)], a well-pronounced maximum at $k = 3.8$ Å^{-1} and $R = 2.3$ Å, and a minor maximum at $k = 7.3$ Å^{-1} and $R = 2.3$ Å exists. With rise of the degree of the chemical disorder, the amplitude of the minor maximum increases and the pronounced maximum is shifted toward higher wave numbers [Fig. 3(b)]. With the further increase of the disorder, two maxima merge and form the wide maximum with an averaged amplitude [Fig. 3(c)]. The nonlinearity of the phase factor [Fig. 1(b)] leads to an artificial rotation of the resulting WT maxima [35]. At the end, such a tendency leads to a single pronounced maximum at $k = 6$ Å^{-1} and $R = 2.3$ Å for the sample with the highest degree of the chemical disorder [Fig. 3(d)].

The interpretation of 2D visualization of the WT could be done by taking into account the k dependence of the backscattering amplitude calculated with FEFF9 [45] and shown in Fig. 1(a). It is clearly seen that the backscattering amplitude of Al has the only maximum at $k = 4.8$ Å^{-1}. Since the k dependence of the backscattering amplitude directly influences the k dependence of the amplitude of EXAFS oscillations $\chi(k)$, the pronounced maximum in the WT of the chemically ordered sample ($B2$ state) in Fig. 3(a) can be attributed to backscattering Al atoms located in the first coordination shell of the absorbing Fe atom. Due to the Fe-rich stoichiometry, in Fe$_{60}$Al$_{40}$ films there is a fraction of Fe atoms surrounded by only Fe nearest neighbors [see Figs. 5(a) and 6(a) for more details], resulting in the minor but visible maximum in Fig. 3(a). This minor maximum occurs at higher k values, as it was expected from Fe scattering paths, since the main maximum of Fe backscattering amplitude is shifted to higher k values.

The number of Fe (Al) backscattering atoms as nearest neighbors rises (vanishes) when the disorder becomes larger in the intermediate $A2$ states and leads to an increased amplitude of the maximum at higher k values associated with Fe sites [see Figs. 3(b) and 3(c)]. For the sample with the highest degree of the disorder (fully disordered $A2$ state), only a single pronounced maximum at $k = 6$ Å^{-1} and $R = 2.3$ Å has been obtained [Fig. 3(d)]. The k value of this single maximum corresponds to the maximum of the backscattering amplitude of bulk Fe. The difference of normalized WT amplitudes for the fully disordered $A2$ state and the ordered $B2$ one is plotted in Fig. 3(e). A positive peak at the k value associated with Fe atoms and a negative one at the k value associated with Al atoms shows an evident growth (descent) of contribution from Fe (Al) atoms into the WT amplitudes through $B2 \rightarrow A2$ transition.

The obtained WT results have directly confirmed that in Fe$_{60}$Al$_{40}$ thin films with an increased chemical disorder induced by Ne$^+$ irradiation the number of Fe (Al) atoms as

nearest neighbors of the Fe absorber increases (decreases), as previously found for Fe$_{60}$Al$_{40}$ alloys [17,18,46,47]. This evolution of the local surrounding is clearly visible in the WT plots and correlates with a formation of larger Fe-rich regions in the fully disordered $A2$ phase.

This information provides first insights into the local surroundings of the absorbing Fe atoms. With these inputs, it is possible to further model the structural changes through the order-disorder transition. The results of such modeling are presented in the next subsection.

2. Refined structural model

The fitting of the experimental EXAFS data has been done by the ARTEMIS [48] program package, which is a graphical front end to the IFEFFIT library including a FEFF code [49]. The calculations were performed on a model FeAl crystal with a structure considering 89 atoms and an initial lattice parameter of 2.86 Å. A cluster radius of 6 Å was chosen.

In the analysis, only scattering paths with an amplitude $>5\%$ of the largest amplitude and with a path length of $\leqslant 5$ Å were taken into account. Multiple-scattering paths were considered as well as the single-scattering ones. For the latter paths, the ratio of Fe and Al atoms in the first coordination shell could be fitted solely within the amplitude factor of the considered paths. The amplitude reduction factor S_0^2 and the energy shift ΔE were set to 0.8 and 3 eV, respectively.

Since both $B2$ and $A2$ phases exhibit cubic symmetry, an isotropic expansion coefficient α was used to fit the spatial distortions $\Delta R = \alpha R_{\mathrm{eff}}$ of Fe and Al atoms, with R_{eff} being an effective path length of each considered scattering path. In order to model the chemical disorder, an EXAFS Debye-Waller factor $\sigma^2 = \sigma_{\mathrm{dyn}}^2 + \sigma_{\mathrm{stat}}^2$ was introduced, where σ_{dyn}^2 refers to dynamic lattice vibrations (at RT in our case) and σ_{stat}^2 accounts for the static disorder. The available data in k space ranges from $k_{\min} = 3.3$ Å^{-1} to $k_{\max} = 12.3$ Å^{-1}, leading to a broad window function with $\Delta k = 9$ Å^{-1} for the Fourier transform. In R space the fitted data ranges from $R_{\min} = 1.5$ Å to $R_{\max} = 5$ Å with $\Delta R = 3.5$ Å. Thus, there are approximately 20 independent variables that are available to fit the experimental data [50].

It was possible to reduce the number of independent variables used in the fitting procedure to only eight. At first, the model system was set up of only the first two coordination shells of the absorbing Fe atoms to fit the experimental data. After that, the model system was extended step by step up to the fifth coordination shell. During the fitting procedure, a variable related to the number of Fe and Al atoms in the coordination shells was first set to a constant while the expansion coefficient α and the Debye-Waller factor σ^2 were fitted. After this, α and σ^2 were fixed and the particular numbers of Fe and Al atoms in each shell were adjusted. In the last step, the amount of Fe and Al atoms in each shell were set to their "best fit" values, whereas α and σ^2 were further fitted repeatedly. The resulting $k\chi(k)$ and $|\mathrm{FT}(k\chi(k))(R)|$ dependencies calculated for Fe local surrounding in accordance with the "best fit" results together with the experimental data for all considered $B2$ and $A2$ states are presented in Fig. 4. An average radial distance and the number of Fe and Al atoms in the first and the second coordination shells around the absorbing Fe atom are
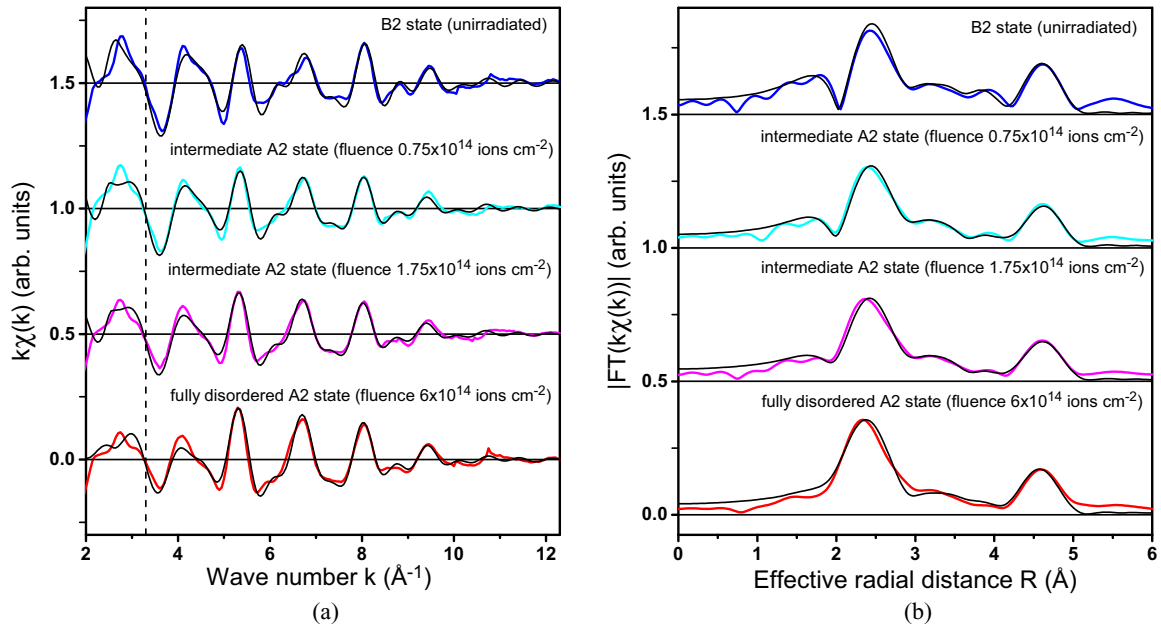
FIG. 4. Experimental data (colored lines) together with fitting results (black lines) of EXAFS oscillations $k\chi(k)$ (a) and related Fourier transforms $|FT(k\chi(k))(R)|$ (not phase corrected) (b) for all studied samples. The curves for different samples are shifted vertically for convenience. The degree of the chemical disorder increases from the top to the bottom. The beginning of the window function used in the FT is showed by the vertical dashed line. The minimum of $|FT(k\chi(k))(R)|$ at $R = 2$ Å becomes less pronounced with increase of the chemical disorder and its magnitude is linked to the number of Al atoms in the first coordination shell of Fe absorber.

summarized in Table I. More details of the fitting procedure are given in Supplemental Material [32].

As follows from Table I, the interpretation of the WT given in the previous subsection is fully consistent with the fit results: In the chemically ordered $B2$ phase, only 3.47(7) Fe atoms were found to be the nearest neighbors of the central absorbing Fe atom, while after the 20-keV Ne^+ ion irradiation with the highest fluence of 6×10^{14} ions cm^{-2} the number of Fe-Fe nearest neighbors was increased up to 5.0(1). Accordingly, the number of Al atoms in the first coordination shell was decreased to fulfill the total number of $N = 8$ nearest neighbors for the bcc structure. In addition, it has been found that the second coordination shell and thereby the lattice parameter was expanded from 2.867(2) to 2.883(4) Å. This increase refers to a volume expansion of $\sim 1\%$. An interpretation of coordination number values is given in the upcoming subsection.

3. Local configurations and relaxed structures

The results of the calculations have revealed a significant difference in local configurations within the first coordination shell around the Fe absorber for $B2$ and $A2$ phases and an increased bond length of its second coordination shell as well. Representative relaxed structures are shown in Figs. 5(a) and 5(b).

The distributions of Fe-Fe nearest neighbors within the supercell for the chosen configurations of the $Fe_{60}Al_{40}$ model crystal are presented in Figs. 6(a) and 6(b). The mean value of each histogram is a measure of an averaged number of Fe-Fe nearest neighbors ($N_{Fe,theory}$) in the particular local configuration, and as follows from Fig. 6 it is visibly shifted to larger values for the fully disordered $A2$ state as expected. The
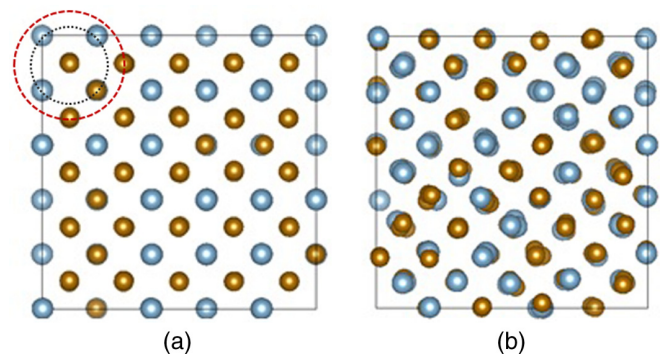
TABLE I. Fitting results for the average distance R_{exp} to the Fe nearest neighbors in the first and second coordination shells, and the numbers of Fe ($N_{Fe,exp}$) and Al ($N_{Al,exp}$) atoms in the first coordination shell.

	Unirradiated sample ($B2$)	Irradiated samples ($A2$)		
Fluence [ions cm^{-2}]		0.75×10^{14}	1.75×10^{14}	6×10^{14}
$R_{exp}^{(1st\ shell)}$ [Å]	2.456(5)	2.468(6)	2.471(6)	2.463(4)
$R_{exp}^{(2nd\ shell)}$ [Å]	2.867(2)	2.874(4)	2.880(5)	2.883(4)
$N_{Fe,exp}$	3.47(7)	4.1(1)	4.6(1)	5.0(1)
$N_{Al,exp}$	4.53(7)	3.9(1)	3.4(1)	3.0(1)

FIG. 5. Relaxed structures for the ordered $B2$ phase (a) and the fully disordered $A2$ phase (b) of an Fe-rich $Fe_{60}Al_{40}$ model crystal (side view). The first and the second coordination shells of Fe atoms are schematically represented by dotted and dashed lines, respectively.
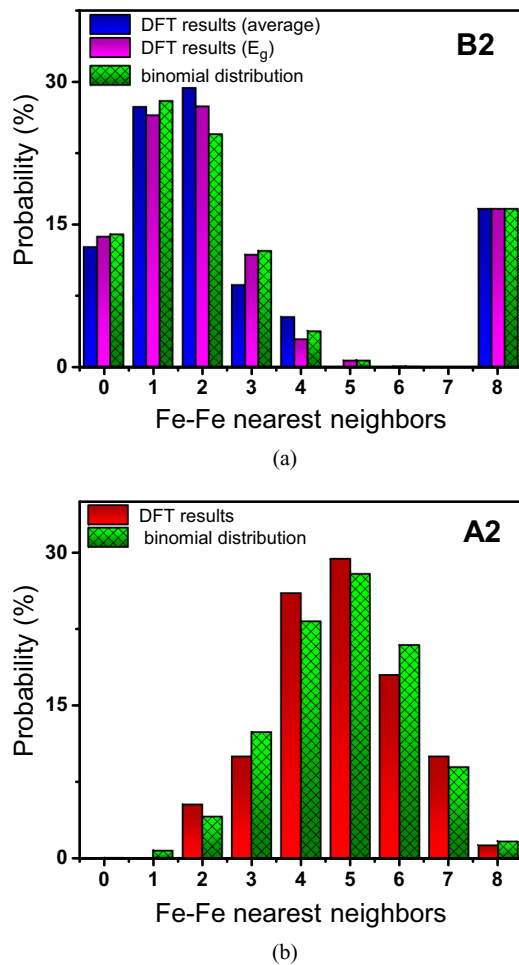
(a)

(b)

FIG. 6. The distributions of Fe-Fe nearest neighbors in the $Fe_{60}Al_{40}$ model crystal for the chemically ordered $B2$ state in the local layer-wise configurations (averaged over all configurations and in the configuration with minimum ground-state energy E_g) (a) and the chemically disordered $A2$ state (b) calculated by VASP. The ideal case of homogeneously distributed disorder is represented by binomial distribution.

presence of eight Fe-Fe nearest neighbors with a probability more than 10% in the ordered $B2$ state [Fig. 6(a)] is a characteristic feature of the particular Fe-rich stoichiometry. The average over all considered configurations for the $B2$ state is shown for a comparison.

The calculated averaged bond lengths between Fe absorber and its neighboring atoms in the first and second coordination shells together with the number of Fe atoms in the first coordination shell for $B2$ and $A2$ states are shown in Table II. The bond length of the second Fe shell (which reflects the lattice parameter) is enlarged from 2.87 Å to 2.89 Å through the $B2 \rightarrow A2$ transition and is in a good agreement with the results of the experimental data fitting in Table I.

For the correct interpretation of obtained values for coordination numbers $N_{Fe,theory}$ and its comparison with $N_{Fe,exp}$ in $B2$ and $A2$ states the site occupancy probabilities should be mentioned. For the ideal bcc binary alloys of $A_x B_{1-x}$ type, local distributions of nearest neighbors in the several first coordination shells can be very well described by binomial

TABLE II. Averaged nearest-neighbor distances from the Fe absorber (R_{theory}) in the first and second coordination shells and the averaged numbers of Fe atoms ($N_{Fe,theory}$) in the first coordination shell calculated by VASP. As uncertainties, the standard errors of mean values are presented in parentheses.

	Chemically ordered state ($B2$)	Chemically disordered state ($A2$)
$R_{theory}^{(1st\ shell)}$ [Å]	2.434(7)	2.449(2)
$R_{theory}^{(2nd\ shell)}$ [Å]	2.864(8)	2.891(4)
$N_{Fe,theory}$	2.67	4.8

distribution of such probabilities. That is a basis in SQS approach for a supercell construction with a further use in different first-principles techniques. The probability P_{nA}^A to have n_A neighboring atoms of a particular A type in the first coordination shell of A atom can be modeled by the probability formula from, e.g., Ref. [51] as

$$P_{nA}^A = q_A B(N, n_A) q_A^{nA} q_B^{(N-nA)},$$

where $q_A = x, q_B = 1 - x$, and $B(N, n) = N!/n!(N - n)!$ are binomial coefficients with $N = 8$ (see also Fig. 6). Accordingly, for the $Fe_{60}Al_{40}$ model alloy with a partial order (the case of the ideal $B2$ structure) the value of the Fe-Fe nearest neighbors is 2.67 ± 0.76 on statistical average, and for a fully random and homogeneously distributed disorder (the ideal $A2$ state) one can get the value of 4.8 ± 1.38. Any deviations from these statistically averaged values for the ideal structures point out a nonhomogeneous probability of site occupancy by Fe and Al atoms. So, the coincidence of coordination number values $N_{Fe,theory}$ (Table II) obtained by VASP with the statistically averaged values is a validation of the supercell construction. Meanwhile, a slight discrepancy obtained between the latter values and experimental $N_{Fe,exp}$ from Table I either for $B2$ or $A2$ states indicates a nonuniform site occupancy by Fe atoms in the studied samples, leading to a preferred formation of Fe-rich regions where an amount of Al atoms is less than predicted by stoichiometry since Fe atoms occupy initially Al sites as well.

For the unirradiated sample ($B2$ state) the value $N_{Fe,exp} = 3.47(7)$ can be related to only a small fraction of such regions in a generally ordered film; for the irradiated sample in the fully disordered $A2$ state with $N_{Fe,exp} = 5.0(1)$ it can be assumed that this fraction is larger. The intermediate $A2$ states reveal a number of Fe-Fe nearest neighbors in the range between two aforementioned values and can be associated with a smooth transition from the partially ordered to the fully disordered states with expanding Fe-rich regions, in agreement with results of the WT analysis. Since ion irradiation can provide in general only a nonhomogeneous disordering inside the entire volume of the film due to a characteristic depth profile of penetrating ions, this interpretation seems to be acceptable.

The obtained structural changes—an increased number of Fe-Fe nearest neighbors and the unit cell expansion—are attributed to be responsible for the long-range ferromagnetic order in the $Fe_{60}Al_{40}$ thin films in the chemically disordered $A2$ phase. Previously reported first-principle theories and effective field theory calculations show that the nearest- and the next-nearest-neighbor Fe-Fe interaction is predominantly
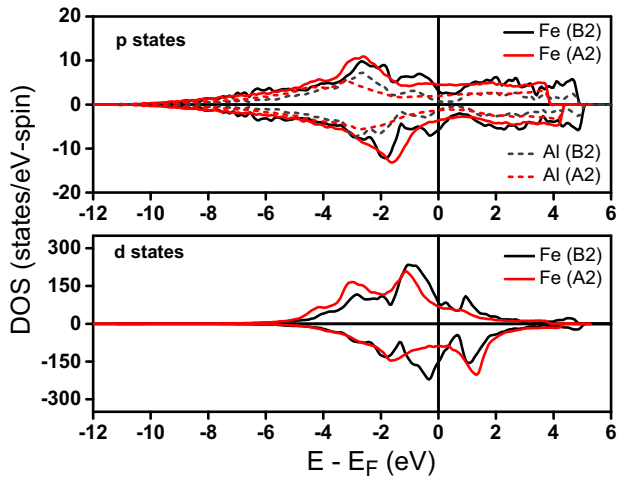
FIG. 7. Spin-resolved DOS for Fe and Al *p* states (top panel) and Fe *d* states (bottom panel) in *B*2 and *A*2 phases calculated by VASP.

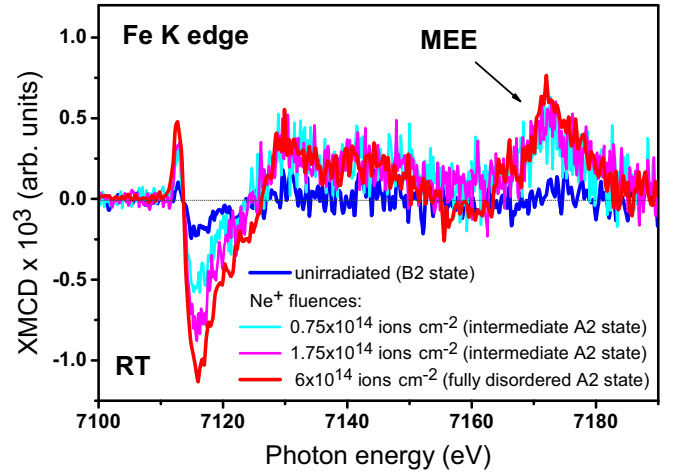

FIG. 8. XMCD spectra for the ordered (*B*2) and the disordered (*A*2) states of $Fe_{60}Al_{40}$ recorded at the Fe K edge at RT; the magnetic MEE peaks are clearly visible only for the *A*2 states.

ferromagnetic [52,53]. An increased number of ferromagnetic Fe-rich regions can be therefore accounted for the macroscopic ferromagnetic state as previously was suggested in Ref. [54] for the $Fe_{60}Al_{40}$ alloy. The increase of the lattice constant is also consistent with results of previously realized band structure calculations [2].

B. Electronic and magnetic properties

1. Density of states and calculated magnetic moments

Spin-resolved densities of states calculated by VASP for Fe and Al atoms in *B*2 and *A*2 phases are shown in Fig. 7. In general, for the Fe-Al system, the shape of DOS and the position of the Fermi energy with respect to bonding-antibonding peaks are determined by the lattice parameter, stoichiometry, and particular local configurations [19,55,56]. In the considered $Fe_{60}Al_{40}$ case, the DOS has a typical structure with well-pronounced peaks and at the Fermi level is dominated by Fe contributions as expected. Well delocalized *p* states of Fe and Al overlap with Fe 3*d* states, making the *p-d* hybridization effective and resulting in non-negligible magnetic moments. The values of related *p* and 3*d* spin magnetic moments are presented in Table III.

TABLE III. Averaged spin magnetic moments (μ_B) for Fe and Al atoms in *B*2 and *A*2 phases calculated by VASP and SPR-KKR.

	Chemically ordered state (*B*2)		Chemically disordered state (*A*2)	
	Fe	Al	Fe	Al
		VASP		
p states	−0.003	−0.010	−0.016	−0.022
d states	0.553		1.420	
		SPR-KKR		
p states	−0.006	−0.017	−0.018	−0.032
d states	0.539		1.391	

Larger splitting of Fe DOS in the fully disordered *A*2 phase leads to substantially larger Fe magnetic moments in comparison with the ordered *B*2 one. This was expected as each Fe atom has on average a larger number of Fe nearest neighbors in the disordered *A*2 phase, thereby increasing the exchange field. We have also found that the magnetic moment in *p* orbitals of Al is comparatively higher for the latter phase. An opposite sign of the Al magnetic moment with respect to the Fe *d* one is in agreement with findings from Refs. [19,20,55]. The averaged spin magnetic moments calculated by SPR-KKR code (see also Table III) are fairly in agreement with ones obtained by VASP and show the same trend of larger moments in the disordered *A*2 state. Moreover, the calculated orbital contribution to Fe total magnetic moment has yielded a value of 0.028 μ_B and 0.068 μ_B for *B*2 and *A*2 phases, respectively.

As follows from Fig. 7, disorder-induced scattering leads to the broadening of DOS for the electronic states, but although spin-resolved DOS of Fe 3*d* states shows broader peaks for the disordered *A*2 phase, the broadening of the total 3*d* DOS is nearly the same for both phases due to a small splitting of Fe nonbonding peak for the ordered *B*2 one.

2. X-ray magnetic circular dichroism

XMCD spectra measured at the Fe K edge are shown in Fig. 8. The structure of the observed XMCD signal around the edge exhibits two characteristic regions: the positive one (around 7112.5 eV) that is a measure of Fe 4*p*-3*d* hybridization strength and the negative one at slightly higher energies (∼7116 eV), which relates mostly to the orbital polarization of Fe 4*p* states [57,58]. In the cubic surrounding, the latter peak amplitude is proportional to the magnetic moment of the absorbing atom [59].

The quadrupolar contribution to the absorption at K edges of 3*d* transition metals [60] in many cases makes a quantitative analysis of magnetic circular dichroism signal not plausible. Qualitatively, the observed XMCD spectra show a significant rise of 4*p*-3*d* iron hybridization via the transition. The comparison with XMCD spectra from Refs. [61,62] (not shown)
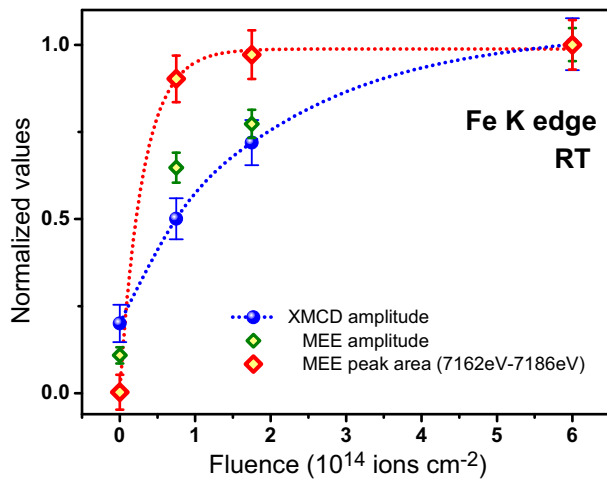
FIG. 9. Fluence dependence of the XMCD and MEE peak amplitude and the integrated MEE signal (7162–7186 eV) for the ordered ($B2$) and the disordered ($A2$) states of $Fe_{60}Al_{40}$ recorded at the Fe K edge at RT. Dotted lines are guides for the eyes.

FIG. 10. Element-specific hysteresis loop measured by XMCD at the Fe K edge (7116 eV) for the sample irradiated with 1.75×10^{14} ions cm^{-2} fluence at two different incident angles as indicated. Symbols represent the experimental data, and dotted lines are the corresponding fits by Langevin function used as guides for eyes. The patterned area relates to the signal instability region.

reveals that $4p$ states orbital magnetic moment and the strength of their hybridization with $3d$ states in the studied $Fe_{60}Al_{40}$ films is smaller than for a pure Fe foil. Furthermore, all XMCD spectra are similar to the spectra of metallic iron, indicating that Ne$^+$ irradiation of the chosen fluences does not induce strong structural deviations from the bcc structure of the initially annealed (unirradiated) $Fe_{60}Al_{40}$ thin film.

Since no visible changes in the spectral shape of XMCD signal were found, the negative XMCD peak amplitude was used to estimate an evolution of the p-state-related magnetic moment with fluence. The normalized amplitudes are shown in Fig. 9. A continuous rise of the magnetic signal with the irradiation fluence was observed. Moreover, the fully disordered sample shows the signal increase with a factor of approximately 4.5 with respect to the ordered one, which is in a reasonable agreement to the calculated magnetic moments.

An example of element-specific magnetization loops measured at the maximum of the XMCD effect (7116 eV) for two incident angles (45° and 90°) is shown in Fig. 10. The full saturation of samples in the chosen experimental geometry as well as preferential in-plane magnetization with almost squared hysteresis is in agreement with macroscopic magnetometry and magneto-optic Kerr effect studies. In the low-field region, an observed signal instability is due to a common problem of detector sensitivity to the secondary electrons emitted from the sample in addition to the fluorescence yield, leading to a strongly disturbed XMCD signal detected by TFY in the case studied.

3. Multielectronic excitation peak

A well-pronounced magnetic MEE peak with a positive amplitude has been found for all studied irradiated samples at the energy around 7172 eV (see Fig. 8). According to detailed studies by Kawamura *et al.* [26,27], the most probable transition associated with this peak is a super-Coster-Kronig-type one described by the final state $(1s)^1(3p)^5(3d)^{n+2}$ resulting from the $3p \rightarrow 3d$ dipole transitions going simultaneously with
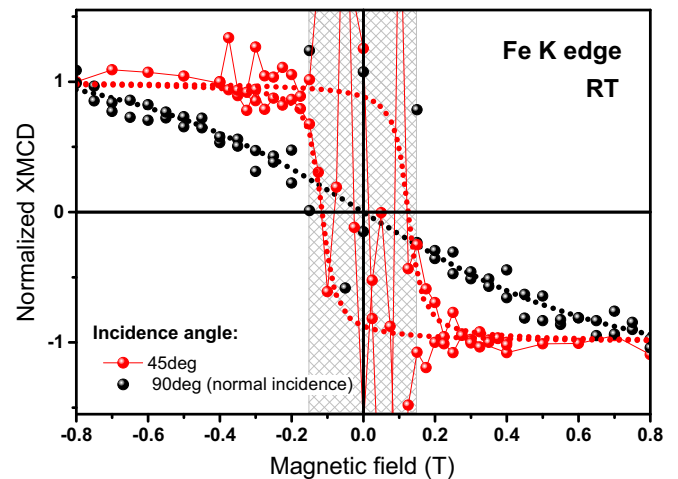
$\epsilon p \rightarrow 3d$ de-excitation. It differs from earlier works [61,63] where $3p \rightarrow 4p$ monopole excitations associated with the $1s \rightarrow 4p$ dipole transitions were suggested. The assumption that the MEE peak is closely related to $3d$ orbitals in transition metals is supported by its energy position, which coincides with the $M_{2,3}$ edges energies of the $(Z + 1)$ atom, by the sign and profile of the dichroic signal, by the dependence of its integrated intensity on the atomic number of the absorbing atoms, and by theoretical calculations [27].

In our work, the position of this MEE peak, its amplitude, and broadening for the considered $A2$ states are similar to what was found earlier for pure Fe [26,61,62]. This suggests the similarity in the electronic structures of Fe $3d$ states in the disordered $Fe_{60}Al_{40}$ films irradiated by fluences larger than 0.75×10^{14} ions cm^{-2} and metallic Fe. In Fig. 9, the fluence dependences of XMCD and MEE normalized amplitudes are presented. Qualitatively, these dependences are in agreement with the common view that the induced orbital polarization of delocalized Fe $4p$ states originates from $3d$ spins through the exchange interaction with $4p$ spin moment and further through a slight spin-orbit coupling of $4p$ states. Interestingly, an integral over magnetic MEE peak has a different tendency (see also Fig. 9): For all studied $A2$ states, its value is almost the same and is much larger than the value obtained for the $B2$ state. Such a difference suggests a prime distinction in $3d$ electronic properties of these two phases.

Since the integral of the magnetic signal over both spin-orbit split edges (e.g., $L_{2,3}$ or $M_{2,3}$) is generally proportional to the orbital magnetic moment of the final states [64,65], the increasing of magnetic MEE peak area can be a sign of an increased $3d$ orbital magnetic moment in agreement to theory results. Another interpretation refers to an almost constant MEE integrated signal in conjunction with a continuously increasing MEE peak amplitude and can be related to an accordingly decreased width of magnetic MEE signal for higher fluences. In general, a narrowing of the XMCD signal for a

weak ferromagnet like Fe can have several reasons like changes in the density of states, exchange splittings, lifetimes of excited states, *etc.* From the calculated spin-resolved DOS, a decrease of the line width caused by a smaller exchange splitting in the disordered phase can be excluded. Besides, by having a closer look to the spin polarization of *d* states above the Fermi energy, which is indirectly related to the MEE XMCD signal, one can see that there is a quite sharp feature around 1.4 eV: The full width of half maximum of the difference between the absolute numbers of spin-down and spin-up states is approximately the same for both *B*2 and *A*2 phases. However, the distinct fine structure of the spin polarization of the *B*2 phase, particularly a smaller maximum close to the Fermi energy, in combination with the instrumental line broadening (∼1.1 eV at 7.1 keV) can explain a broader MEE XMCD signal for the ordered state. An additional influence of different lifetimes cannot be excluded. In contrast, the DOS and the spin polarization of the *p* states above the Fermi energy are rather smooth. Therefore, taking the amplitude of the K-edge XMCD instead of the integrated signal is still a valid approximation to estimate the magnetic moment fluence dependence.

These results indicate that the electronic structure of $Fe_{60}Al_{40}$ system is very sensitive to induced disorder, in agreement to detailed theoretical studies by Das *et al.* [55], where it was obtained that even subtle changes in *p-d* hybridization affect the chemical bonding between Fe and Al due to its short-range character. Thus, a variation in 3*d* states localization could be expected as a consequence of changes in Fe local environment: As follows from Table I, for higher fluences fewer Al neighbors stay in the first coordination shell of Fe absorbers, leading to a smaller antibonding effect of Fe 3*d*–Al *p* hybridization. For the *B*2 state, a weaker localization is expected due to a larger amount of neighboring Al atoms. More precise comparison between theory and experiment would need theoretical studies considering an additional core hole in accordance with Coster-Kronig-type transitions, which may significantly influence the results of DOS calculations, as well as experimental data with better statistics to draw quantitative conclusions about 3*d* states localization on the basis of the MEE intensity. However, answering that question is beyond the scope of this work.

For thin films with another electronic structure of components, the relation between structural and/or chemical disorder and magnetic short- or long-range ordering is expected to be different due to, e.g., a larger amount of electrons participates in the hybridization process, different influences of initial *d* and *p* states localization, other electronegativities of the constituents, different unit cell changes, etc. These factors would determine a rise or drop of magnetization depending on the degree of disordering. To unravel the exact scenario of the phase transition initiated by ion irradiation, element-specific studies with hard x rays are a method of choice.

IV. CONCLUSIONS

Ion-beam irradiation with low fluences is a very effective tool for the creation of different magnetic structures in a controlled way. Variation of the irradiation fluence and ion energy could be used to adjust the magnetic properties of thin films with different thicknesses continuously, whereas a local

chemical disorder influences the ferromagnetic ordering on a macroscopic scale. To understand the formation mechanism of such a long-range ferromagnetic order and to find its characteristic peculiarities, the detailed studies of local structural changes inside the film are needed.

In our work, a clear evolution of the local environment around Fe atoms and Fe orbital polarizations in $Fe_{60}Al_{40}$ thin films has been observed by the element-specific hard x-ray absorption spectroscopy along the order-disorder ($B2 \rightarrow A2$) phase transition initiated by 20-keV Ne^+ ion irradiation. An increase of the chemical disorder induced by ion fluences of $(0.75-6) \times 10^{14}$ ions cm^{-2} is evidently reflected in consequential changes of structural and magnetic properties of the studied $Fe_{60}Al_{40}$ films of 40 nm thickness.

The analysis of EXAFS spectra recorded at the Fe K edge at room temperature has shown the clear rearrangement in the first coordination shell of Fe absorbers through the transition with the increased number of Fe-Fe nearest neighbors from 3.47(7) to 5.0(1) and the unit cell volume expansion of ∼1%. A model system for a proper fitting of the experimental data has been built on the basis of prior information about the predominant type of atoms in the local Fe coordination taken from the wavelet transforms. The deviations of obtained numbers of Fe-Fe nearest neighbors from the averaged numbers of those calculated for the ideal binary alloy with randomly apportioned disorder (2.67 and 4.8, respectively) assume the preferential formation of Fe-rich regions around Fe atoms in the films studied. The fraction of these regions becomes larger with fluence increasing.

The XMCD signal associated with $1s \rightarrow 4p$ dipole transitions probed at the Fe K edge at RT has shown a continuous rise of Fe 4*p* orbital polarization and an increased strength of its 4*p*-3*d* interatomic hybridization with increase of the irradiation fluence while keeping the spectral shape similar to the spectra of the metallic iron. The obtained quantities are smaller than those for a pure Fe foil. The pronounced magnetic MEE peak assigned to the $3p \rightarrow 3d$ super-Coster-Kronig-type transitions has been found for all studied *A*2 phases at ∼60 eV above the Fe K edge. The different tendencies of magnetic MEE peak amplitude and its integrated area suggest an increase of 3*d* states orbital magnetic moments for *A*2 phases with fluence increasing, while a similarity in fluence dependencies of magnetic MEE and XMCD peak amplitudes is in agreement with a view that Fe 4*p* orbital moment follows Fe 3*d* spin polarization through exchange and spin-orbit interactions. A strong influence of the local surrounding rearrangement on the electronic and magnetic properties of Fe 3*d* states that are further reflected in orbital polarization of Fe 4*p* states has been revealed.

First-principles density functional calculations by the VASP program package revealed strong distinctions in local geometries of Fe and Al atoms for the ordered (*B*2) and disordered (*A*2) phases while both of them are close to binomial distributions of site occupancy probability for the ideal $Fe_{60}Al_{40}$ case in the aforementioned phases. The enlarged number of Fe-Fe nearest neighbors and the enlarged lattice constant has been found for the chemically disordered *A*2 state contrary to the ordered *B*2 one, in agreement with the experimental findings and previous reports. Spin-resolved DOS demonstrated a typical shape for Fe *d* states and the expected delocalized nature of Fe and Al *p* states with a larger

splitting for the disordered phase for both types of orbitals. The calculated magnetic moments showed an evident enlargement for the $A2$ phase, correspondingly. The same tendency with increased magnetic moments has been found by the KKR-CPA approach.

These structural findings together with XMCD results support the idea that the formation of larger Fe-rich regions in the disordered $A2$ phase of $Fe_{60}Al_{40}$ thin films gives rise to a macroscopic ferromagnetic state. Intuitively, details of structural rearrangements, orbital magnetism, and peculiarities in hybridization of d and p states due to changes in the local environment play a significant role either in formation of the disorder-induced ferromagnetic state or destroying the initial ferromagnetic order for other alloys also. On a local scale, these changes could be probed simultaneously by element-specific XAS (including EXAFS, XMCD, and magnetic MEE) at K absorption edges for all $3d$ transition metals. Particular studies of magnetic effects depending on the degree of the chemical disorder and the electronic structure of alloys constituent components will allow one to understand more deeply underlying mechanisms of the disorder-induced ferromagnetism phenomenon that will be exploited in further development of modern technology.

ACKNOWLEDGMENTS

[1] C. Chappert, H. Bernas, J. Ferré, V. Kottler, J.-P. Jamet, Y. Chen, E. Cambril, T. Devolder, F. Rousseaux, V. Mathet, and H. Launois, Science **280**, 1919 (1998).

[2] J. Nogués, E. Apiñaniz, J. Sort, M. Amboage, M. d'Astuto, O. Mathon, R. Puzniak, I. Fita, J. S. Garitaonandia, S. Suriñach *et al.*, Phys. Rev. B **74**, 024407 (2006).

[3] J. Fassbender and J. McCord, J. Magn. Magn. Mater. **320**, 579 (2008).

[4] *Magnetic Properties of Metals Alloys and Compounds of d-Elements with Main Group Elements. Part 1*, Landolt-Börnstein - Group III Condensed Matte, edited by H. P. J. Wijn (Springer, Berlin, 1987), Vol. 19B, p. 323.

[5] J. Wolff, M. Franz, A. Broska, B. Köhler, and T. Hehenkamp, Mater. Sci. Eng.: A **239–240**, 213 (1997).

[6] A. Hernando, X. Amils, J. Nogués, S. Suriñach, M. D. Baró, and M. R. Ibarra, Phys. Rev. B **58**, R11864 (1998).

[7] J. Bogner, W. Steiner, M. Reissner, P. Mohn, P. Blaha, K. Schwarz, R. Krachler, H. Isper, and B. Sepiol, Phys. Rev. B **58**, 14922 (1998).

[8] R. Bali, S. Wintz, F. Meutzner, R. Hübner, R. Boucher, A. A. Ünal, S. Valencia, A. Neudert, K. Potzger, J. Bauch *et al.*, Nano Lett. **14**, 435 (2014).

[9] J. Sort, A. Concustell, E. Menéndez, S. Suriñach, K. V. Rao, S. C. Deevi, M. D. Baró, and J. Nogués, Adv. Mater. **18**, 1717 (2006).

[10] E. Menéndez, J. Sort, M. O. Liedke, J. Fassbender, S. Suriñach, M. D. Baró, and J. Nogués, New J. Phys. **10**, 103030 (2008).

[11] J. Fassbender, M. O. Liedke, T. Strache, W. Möller, E. Menéndez, J. Sort, K. V. Rao, S. C. Deevi, and J. Nogués, Phys. Rev. B **77**, 174430 (2008).

[12] E. Menéndez, M. O. Liedke, J. Fassbender, T. Gemming, A. Weber, L. J. Heyderman, K. V. Rao, S. C. Deevi, S. Suriñach, M. D. Baró *et al.*, Small **5**, 229 (2009).

[13] J. Ehrler, M. He, M. V. Shugaev, N. I. Polushkin, S. Wintz, V. Liersch, S. Cornelius, R. Hübner, K. Potzger, J. Lindner *et al.*, ACS Appl. Mat. Interfaces **10**, 15232 (2018).

[14] N. Tahir, R. Bali, R. Gieniusz, S. Mamica, J. Gollwitzer, T. Schneider, K. Lenz, K. Potzger, J. Lindner, M. Krawczyk *et al.*, Phys. Rev. B **92**, 144429 (2015).

[15] N. Tahir, R. Gieniusz, A. Maziewski, R. Bali, M. Kostylev, S. Wintz, H. Schultheiss, S. Facsko, K. Potzger, J. Lindner, and J. Fassbender, IEEE Trans. Magn. **50**, 1 (2014).

[16] G. K. Wertheim, V. Jaccarino, J. H. Wernick, and D. N. E. Buchanan, Phys. Rev. Lett. **12**, 24 (1964).

[17] G. P. Huffman and R. M. Fisher, J. Appl. Phys. **38**, 735 (1967).

[18] E. Yelsukov, E. Voronina, and V. Barinov, J. Magn. Magn. Mater. **115**, 271 (1992).

[19] N. I. Kulikov, A. V. Postnikov, G. Borstel, and J. Braun, Phys. Rev. B **59**, 6824 (1999).

[20] B. Reddy, P. Jena, and S. Deevi, Intermetallics **8**, 1197 (2000).

[21] T. Sikora, M. Jaouen, T. Girardeau, and J. Mimault, Nucl. Instr. Methods Phys. Res. B **111**, 141 (1996).

[22] E. V. Voronina, T. Miyanaga, S. Nagamatsu, T. Fujikawa, and L. V. Dobysheva, J. Surf. Invest. **3**, 343 (2009).

[23] I. Arčon, M. Mozetič, A. Zalar, A. Kodre, and J. Jagielski, Nucl. Instr. Methods Phys. Res. B **199**, 222 (2003).

[24] C. Antoniak, Beilstein J. Nanotechnol. **2**, 237 (2011).

[25] A. Rogalev and F. Wilhelm, Phys. Met. Metallogr. **116**, 1285 (2015).

[26] N. Kawamura, H. Maruyama, K. Kobayashi, S. Uemura, A. Urata, and H. Yamazaki, J. Phys. Soc. Jpn. **68**, 923 (1999).

[27] N. Kawamura, T. Yamamoto, H. Maruyama, I. Harada, M. Suzuki, and T. Ishikawa, J. Synchrotron Radiat. **8**, 410 (2001).

[28] V. Sundararajan, B. R. Sahu, D. G. Kanhere, P. V. Panat, and G. P. Das, J. Phys.: Condens. Matter **7**, 6019 (1995).

[29] J. Zou and C. L. Fu, Phys. Rev. B **51**, 2115 (1995).

[30] V. L. Moruzzi, A. R. Williams, and J. F. Janak, Phys. Rev. B **10**, 4856 (1974).

[31] C. Müller, W. Blau, and P. Ziesche, Phys. Status Solidi B **116**, 561 (1983).

[32] See Supplemental Material at http://link.aps.org/supplemental/10.1103/PhysRevB.98.024101 for more details of the EXAFS fitting procedure.

[33] D. E. Sayers, E. A. Stern, and F. W. Lytle, Phys. Rev. Lett. **27**, 1204 (1971).

[34] J. J. Rehr and R. C. Albers, Rev. Mod. Phys. **72**, 621 (2000).

[35] H. Funke, A. C. Scheinost, and M. Chukalina, Phys. Rev. B **71**, 094110 (2005).

[36] M. O. Liedke, W. Anwand, R. Bali, S. Cornelius, M. Butterling, T. T. Trinh, A. Wagner, S. Salamon, D. Walecki, A. Smekhova *et al.*, J. Appl. Phys. **117**, 163908 (2015).

[37] A. Rogalev, F. Wilhelm, J. Goulon, and G. Goujon, Advanced Instrumentation for x-ray Magnetic Circular Dichroism, Magnetism and Synchrotron Radiation: Towards the Fourth Generation Light Sources, in *Proceedings of the 6th International School "Synchrotron Radiation and Magnetism"*, edited by E. Beaurepaire, H. Bulou, L. Joly, and F. Scheurer, Mittelwihr (France), 2012, Part of the Springer Proceedings in Physics Vol. 151 (Springer, 2013), pp. 289–314.

[38] G. Kresse and J. Hafner, Phys. Rev. B **47**, 558 (1993).

[39] G. Kresse and J. Furthüller, Comput. Mater. Sci. **6**, 15 (1996).

[40] G. Kresse and J. Furthmüller, Phys. Rev. B **54**, 11169 (1996).

[41] G. Kresse and D. Joubert, Phys. Rev. B **59**, 1758 (1999).

[42] J. Korriga, Physica (Amsterdam, Neth.) **13**, 392 (1947).

[43] W. Kohn and N. Rostoker, Phys. Rev. **94**, 1111 (1954).

[44] A. Zunger, S.-H. Wei, L. G. Ferreira, and J. E. Bernard, Phys. Rev. Lett. **65**, 353 (1990).

[45] J. Rehr, J. Kas, F. Vila, M. Prange, and K. Jorissen, Phys. Chem. Chem. Phys. **12**, 5503 (2010).

[46] E. A. Friedman and W. J. Nicholson, J. Appl. Phys. **34**, 1048 (1963).

[47] P. Beck, Metall. Mater. Trans. B **2**, 2015 (1971).

[48] B. Ravel and M. Newville, J. Synchrotron Radiat. **12**, 537 (2005).

[49] M. Newville, J. Synchrotron Radiat. **8**, 96 (2001).

[50] P. A. Lee, P. H. Citrin, P. Eisenberger, and B. M. Kincaid, Rev. Mod. Phys. **53**, 769 (1981).

[51] D. D. Johnson and F. J. Pinski, Phys. Rev. B **48**, 11553 (1993).

[52] D. Dias, J. R. de Sousa, and J. Plascak, Phys. Lett. A **373**, 3513 (2009).

[53] T. Ghosh, A. P. Jena, and A. Mookerjee, J. Alloys Compd. **639**, 583 (2015).

[54] L. E. Zamora, G. A. Pérez Alcázar, G. Y. Vélez, J. D. Betancur, J. F. Marco, J. J. Romero, A. Martínez, F. J. Palomares, and J. M. González, Phys. Rev. B **79**, 094418 (2009).

[55] G. P. Das, B. K. Rao, P. Jena, and S. C. Deevi, Phys. Rev. B **66**, 184203 (2002).

[56] E. Apiñaniz, F. Plazaola, and J. Garitaonandia, Eur. Phys. J. B **31**, 167 (2003).

[57] G. Y. Guo, J. Phys.: Condens. Matter **8**, L747 (1996).

[58] H. Ebert, J. Stöhr, S. S. P. Parkin, M. Samant, and A. Nilsson, Phys. Rev. B **53**, 16067 (1996).

[59] J.-I. Igarashi and K. Hirai, Phys. Rev. B **50**, 17820 (1994).

[60] G. Y. Guo, Phys. Rev. B **55**, 11619 (1997).

[61] S. Pizzini, A. Fontaine, E. Dartyge, C. Giorgetti, F. Baudelet, J. P. Kappler, P. Boher, and F. Giron, Phys. Rev. B **50**, 3779 (1994).

[62] O. Mathon, F. Baudelet, J.-P. Itié, S. Pasternak, A. Polian, and S. Pascarelli, J. Synchrotron Radiat. **11**, 423 (2004).

[63] E. Dartyge, F. Baudelet, C. Brouder, A. Fontaine, C. Giorgetti, J. Kappler, G. Krill, M. Lopez, and S. Pizzini, Physica B (Amsterdam, Neth.) **208**, 751 (1995).

[64] B. T. Thole, P. Carra, F. Sette, and G. van der Laan, Phys. Rev. Lett. **68**, 1943 (1992).

[65] P. Carra, B. T. Thole, M. Altarelli, and X. Wang, Phys. Rev. Lett. **70**, 694 (1993).